PHYSICAL SCIENCES

Plasmonic tuning of dark-exciton radiation dynamics and far-field emission directionality in monolayer WSe_2

Shuaiyu Jin[1], Feihong Liu[1], Ilya Razdolski[1,2], Tsz Wing Lo[3], Yaorong Wang[1], Zhiwei Peng[1], Kuan Liang[4], Ye Zhu[4], Wang Yao[5,6], Anatoly V. Zayats[3], Dangyuan Lei[1,7]*

Manipulation of excitonic emission properties is important for numerous photonic applications. Of particular interest are developing easy-to-implement yet effective approaches for controlling the radiation dynamics and directionality of spin-forbidden dark excitons (X_D) in two-dimensional semiconductors. Here, we investigate the spectral, temporal, and directional characteristics of room-temperature X_D emission from a tungsten diselenide monolayer coupled to a dissipative plasmonic nanocavity. Under resonant plasmon-exciton coupling, the radiative decay rate of X_D is accelerated by nearly four orders of magnitude, and correspondingly, the X_D lifetime is shortened to a subnanosecond level, making it comparable to that of bright excitons. Fitting the measured lifetimes with a Purcell-formalism–based cavity quantum electrodynamics model allows estimating of the intrinsic room-temperature X_D lifetime to be about 24 ± 2.3 microseconds. Furthermore, the measured radiation patterns of the dark excitons show that subtle variations in the nanocavity orientation can effectively tailor the X_D emission directionality, important for quantum technologies and optoelectronics applications.

INTRODUCTION

In monolayer transition metal dichalcogenides (ML TMDCs), the lack of inversion symmetry and strong spin-orbit coupling result in spin splitting of the conduction band, typically on the order of a few tens of milli–electron volt. This leads to the spin-valley coupling of electronic bands at the K and K′ valleys (*1*, *2*). Within each spin-split conduction band, electrons with opposite spins can interact with holes in the corresponding valence bands through Coulomb attraction. These interactions give rise to spin-allowed bright excitons (X_O) and spin-forbidden dark excitons (X_D) (*3*, *4*). Group theory analysis has demonstrated that the transition dipole orientations of X_O and X_D are perpendicular to each other (*5*, *6*). In addition, X_D exciton exhibits a significantly longer lifetime compared to X_O exciton due to the selection rules because the optical transition of X_D exciton requires a spin-flip process (*7*, *8*). Previous research has indicated that the lifetime of X_D excitons is two orders of magnitude longer than that of X_O ones at cryogenic temperature (~10 K) (*9*). However, the lifetime difference between X_D and X_O at room temperature remains unclear, as X_D exciton emission is typically undetectable under these conditions.

The rate of excitonic transitions is governed by both the dipole strength of the optical transition and the local density of optical states, as described by Fermi's golden rule. Accordingly, two principal strategies have emerged to enhance X_D emission. The first one involves enabling a nonzero dipole moment D of the relevant optical transition through a magnetic field–induced spin mixing (*6*, *10*–*12*). The second approach focuses on increasing the local density of optical states by coupling the excitonic emitter to optical cavities. Plasmonic nanostructures have been shown to markedly accelerate forbidden transitions in molecules, exploiting associated strongly inhomogeneous fields (*12*), and this mechanism can be used for controlling X_D emission in two-dimensional (2D) materials. The emission of X_D can be enhanced by coupling with either propagating surface plasmon polaritons on a metal film at cryogenic temperatures (*13*) or localized surface plasmons (LSP) in nanocavities formed by a tip (*8*) or a nanoparticle-on-mirror structure (*14*). Both approaches have already paved the way for further applications of X_D excitons in nanoscale devices. However, the underlying mechanism and characteristics of both magnetic field–induced and plasmon-enhanced X_D emission remain unexplored, not to mention the possibility of further manipulating its properties.

In this work, we use a class of ultracompact gold nanocube-on-mirror (NCoM) cavities with tunable plasmon resonance to manipulate the room-temperature emission properties of X_D excitons in monolayer WSe_2, focusing on the corresponding radiation dynamics and directionality. We observe a giant X_D emission enhancement from the WSe_2-NCoM hybrid structure and a marked reduction of the room-temperature X_D lifetime to a subnanosecond level, comparable to that of the spin-allowed X_O (~450 ps). Tuning the energy difference between X_D exciton and the nanocavity gap-plasmon mode enables systematic manipulation of the X_D emission intensity and lifetime. Using a quantum electrodynamics model based on the Purcell formalism for dissipative cavities to fit the measured lifetimes, we estimate the intrinsic room-temperature lifetime of X_D to be 24 ± 2.3 μs, corresponding to a Purcell factor of 3×10^4 for the hybrid structure. Back-focal-plane (BFP) images of the X_D emission coupled to nanocavities reveal a series of highly distorted donut-shaped patterns, resulting from the redistribution of Purcell factor hotspots within the nanoscale cube-mirror gap (induced by slight tilting of the nanocavity) and the spatially dependent radiation patterns of emitters across the nanogap. The obtained results hold promise in advancing the applications of spin-forbidden X_D in quantum technologies and nanoscale optoelectronics (*15*, *16*).

[1]Department of Materials Science and Engineering, City University of Hong Kong, Hong Kong S.A.R. 999077, China. [2]Photonics Research Centre, Universiti Malaya, 50603 Kuala Lumpur, Malaysia. [3]Department of Physics and London Centre for Nanotechnology, King's College London, Strand, London WC2R 2LS, UK. [4]Department of Applied Physics, Research Institute for Smart Energy, The Hong Kong Polytechnic University, Hung Hom, Hong Kong S.A.R. 999077, China. [5]New Cornerstone Science Laboratory, Department of Physics, The University of Hong Kong, Hong Kong S.A.R. 999077, China. [6]Hong Kong Institute of Quantum Science & Technology, The University of Hong Kong, Hong Kong S.A.R. 999077, China. [7]Department of Physics, Centre for Functional Photonics, Hong Kong Branch of National Precious Metals Material Engineering Research Centre, and Hong Kong Institute of Clean Energy, City University of Hong Kong, Hong Kong S.A.R. 999077, China.
*Corresponding author. Email: dangylei@cityu.edu.hk

Results, design, and characterization of coupled WSe_2-NCoM nanocavities

A WSe_2 monolayer was placed in an ultracompact (gap width ~ 1.8 nm) plasmonic NCoM cavity formed by a gold film and a gold nanocube (Fig. 1B; see Materials and Methods for the details of the fabrication). The related cavity plasmon mode features a strongly confined out-of-plane electric field that couples to dipole moments of the excitons (Fig. 1A).

The dark-field scattering spectrum reveals three plasmonic resonance modes of the WSe_2-NCoM hybrid system: the out-of-plane gap plasmon mode I centered at ~1.60 eV; another out-of-plane mode II centered at ~1.93 eV with a much stronger localized electric field centered at ~1.93 eV, which makes it inapplicable for efficient resonant coupling with the X_D exciton (*17*); and the in-plane transverse mode III centered at ~2.35 eV (Fig. 1C). The inset in Fig. 1B shows the distribution of the out-of-plane electric field component for mode I. This field E_z is notably stronger than the in-plane components and asymmetric due to oblique incidence (fig. S3). By optimizing the nanocube size (~85-nm edge length) and the Au mirror thickness (~100 nm), we can tune the resonance energy of the gap

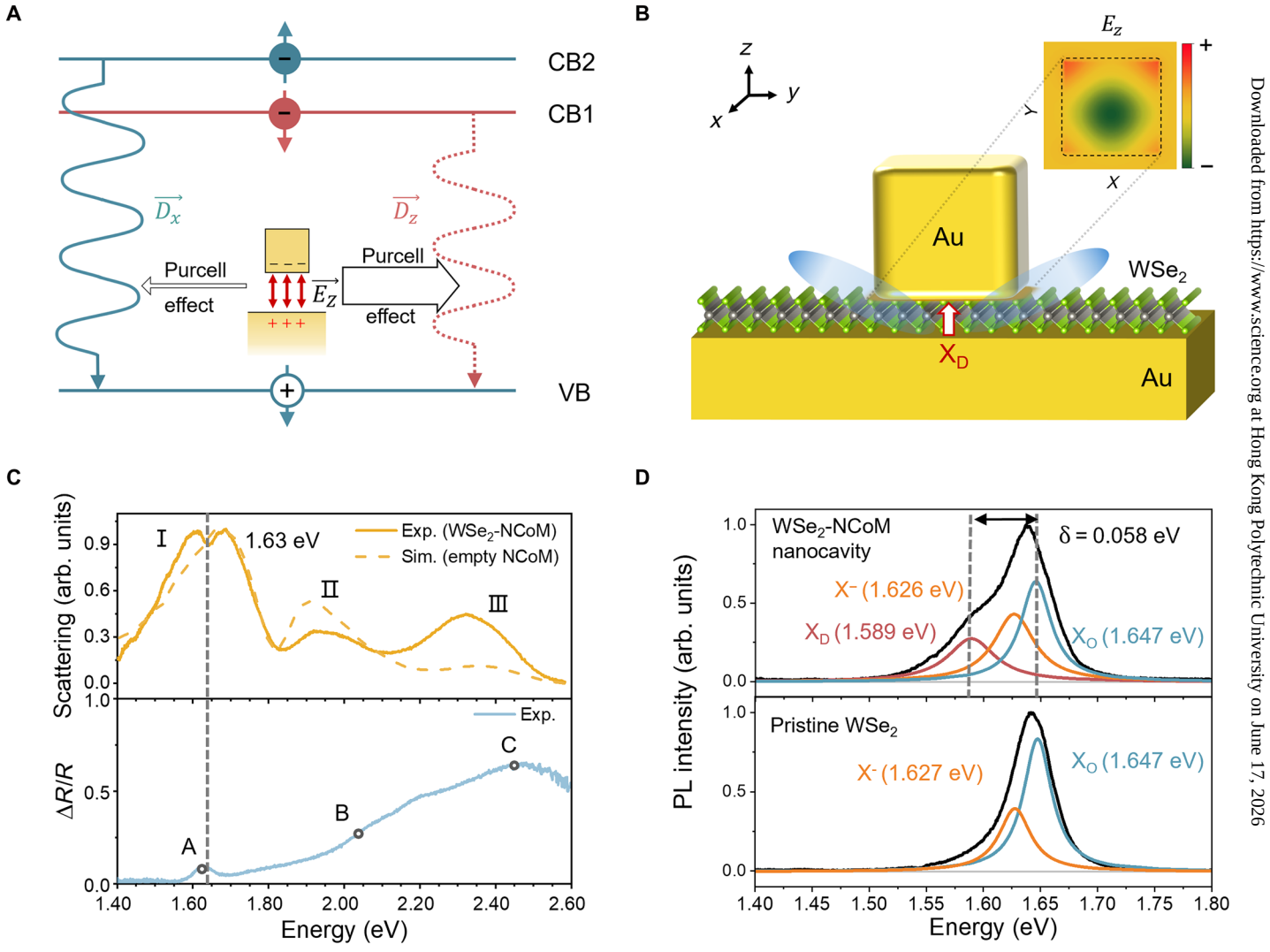

Fig. 1. NCoM nanocavity–induced emission of X_D. (**A**) Energy band diagram of ML WSe_2 at the K valley. As indicated by the red and blue arrows, electrons in the lower (CB1) and higher (CB2) conduction bands have opposite spins, giving rise to an optically bright exciton state with an in-plane dipole moment (X_O) and an optically dark exciton state with an out-of-plane dipole moment (X_D). VB indicates the upper valence band. (**B**) Schematic illustration of the WSe_2-NCoM cavity. The red arrow represents the out-of-plane X_D dipole, which is coupled with the vertical gap plasmon mode of NCoM. The inset shows the calculated distribution of an out-of-plane component of the electric field in NCoM at the gap plasmon resonance (~1.65 eV). (**C**) Top: Dark-field scattering spectrum (solid line) of a single WSe_2-NCoM cavity under white light illumination. The dashed line shows the simulated scattering spectra of the NCoM cavity without WSe_2 ML. The dip at around 1.65 eV in the WSe_2-NCoM cavity spectra originates from the weak coupling between the gap plasmon mode and the X_O exciton state in WSe_2. Bottom: A spectrum of differential reflectance $\frac{\Delta R}{R} = \frac{R_2 - R_1}{R_2}$ of a pristine WSe_2 ML, where R_1 and R_2 are the reflectance values of the Au mirror with and without the WSe_2 ML, respectively. A, B, and C indicate the energies of bright exciton states. arb., arbitrary; Exp., experiment; Sim., simulation. (**D**) Top: Photoluminescence (PL) spectrum measured under the 532-nm excitation from a single WSe_2-NCoM cavity (black), overlaid with three Lorentzian fit curves showing the presence of X_O (blue), X^--trion (orange), and X_D (red) emission. Bottom: PL spectra of a pristine WSe_2 ML, overlaid with two Lorentzian fit curves showing the presence of (blue) X_O and (orange) X^--trion emission only.

plasmon mode I to the energy of X_D (~1.59 eV). Furthermore, the scattering spectrum of a WSe_2-NCoM shows a dip in the vicinity of mode I, which, according to the differential reflectivity data of a bare WSe_2 monolayer, can be attributed to the weak coupling between the X_O and the resonant gap plasmon mode with the resulting spectrum being the addition of the individual spectra of the cavity and the exciton, which are slightly shifted with respect to each other (Fig. 1C) (*18*, *19*).

The emission spectrum of WSe_2-NCoM is dominated by the prominent bright exciton emission peak centered at ~1.65 eV (Fig. 1D), accompanied by a broad shoulder in the lower energy range. Similar results were obtained on another sample where the WSe_2 layer outside of the cavity was removed by reactive ion etching (fig. S5), thus confirming the pivotal role of the NCoM cavity coupling for the X_D emission. In contrast, the photoluminescence (PL) spectrum of the bare WSe_2 monolayer shows the emission from the bright excitons X_O and trions X^- without additional notable features (Fig. 1D). The PL spectrum in the top panel of Fig. 1D uses three Lorentzians corresponding to the X_O (blue), trion (orange), and X_D (red) exciton states. Notably, the X_O and trion energies closely match the respective exciton energies in the bare WSe_2 monolayer. The energy difference between X_O and X_D is ~58 meV, in agreement with previous reports (*9*, *14*). The fitting results show that the X_D linewidth (~54 meV) is larger than that of the X_O (~32 meV), which might be attributed to the inhomogeneous contribution brought by the gold film (*20*) and the plasmon-exciton coupling–induced decrease in the PL quantum yield (*21*).

Further insights into the emission properties of the nanocavities can be obtained by tuning the LSP resonance away from the exciton band. To understand the effect of spectral detuning and its impact on the intensities and lifetime of X_D exciton, we examined 14 WSe_2-NCoM nanocavities (fig. S8). Figure 2A shows dark-field scattering spectra of five representative WSe_2-NCoM nanocavities, each exhibiting a different energy detuning between the plasmon mode and X_D resonance. The detuning was achieved through the subtle size variations of individual nanocubes, resulting in the different resonance frequencies of mode I in Fig. 1C. The detuning energy can be estimated from the scattering spectra using the fitting with the coupled oscillator model (*22*). The dispersion of X_O and the plasmon mode extracted from the model are shown in fig. S9, revealing no avoided crossing (Rabi splitting). The corresponding PL spectra are shown in Fig. 2B, with three Lorentzian

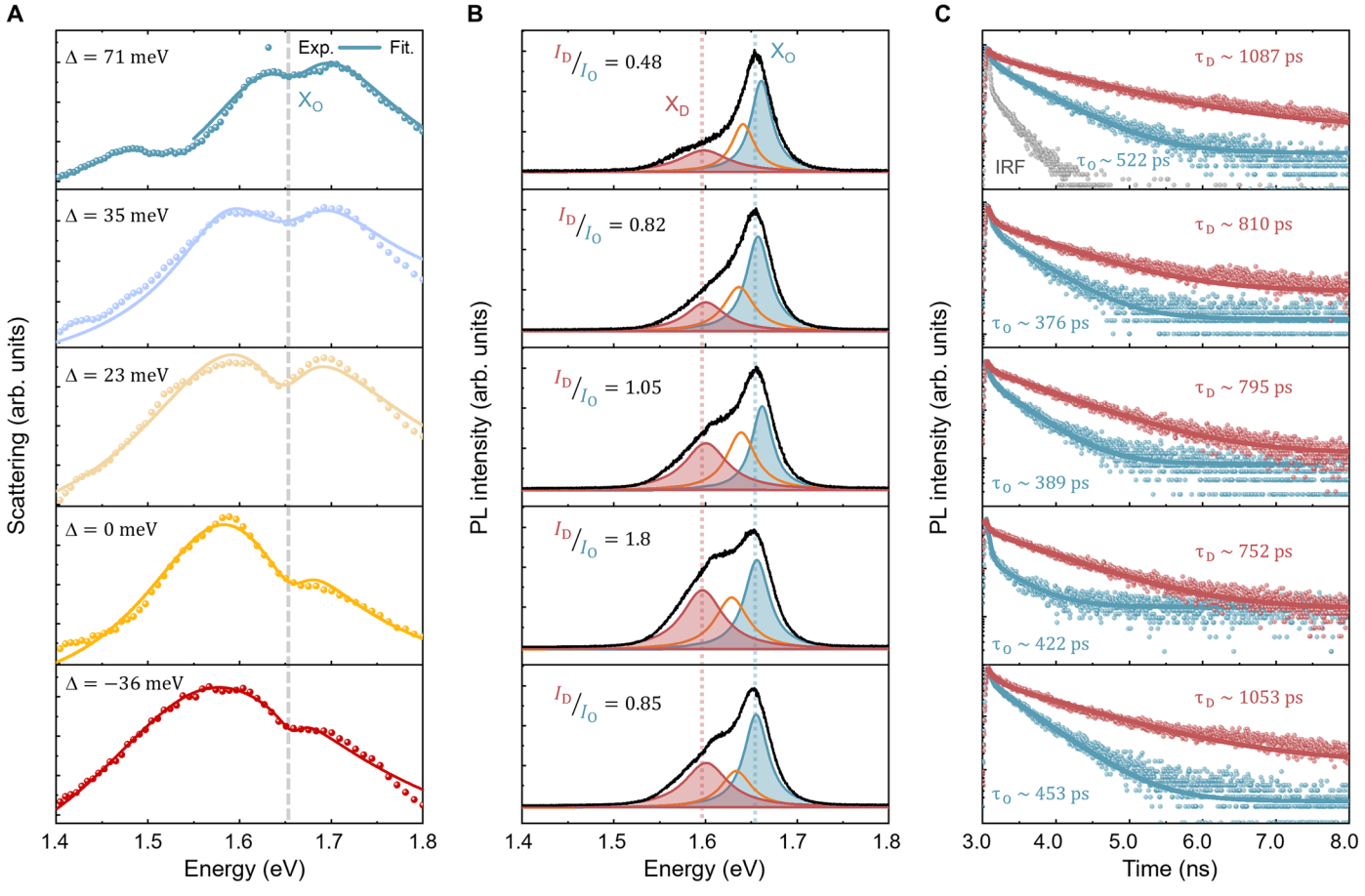

Fig. 2. Dark-field scattering, PL, and TRPL responses of WSe_2-NCoM nanocavities. (**A**) Dark-field scattering spectra for different gap plasmon mode resonances as indicated by various detuning (D) between the energy of the gap plasmon mode (E_P) and the energy of the X_D exciton (E_D). Symbols represent experimental results, and lines are fitting results by a coupled-oscillator model. The gray dashed line indicates the energy of bright excitons. Fit., fitting. (**B**) Corresponding PL spectra, overlaid with three Lorentzian fit curves. $\frac{I_D}{I_O}$ is the peak area ratio of X_D to X_O. The red (blue) dotted line represents the peak energy of X_D (X_O) exciton. (**C**) Corresponding TRPL responses of X_D (red dots) and X_O excitons (blue dots). Gray dots are the instrument response function (IRF). The solid lines represent biexponential fitting.

fits used to extract the peak areas of X_D, X^-, and X_O. The peak area ratio of X_D to X_O emission first increases and then decreases, as the gap plasmon mode shifts from red detuned to blue detuned relative to the X_D energy. Similar trends were observed at low temperature (150 K; fig. S10). Time-resolved PL (TRPL) measurements in Fig. 2C reveal the lifetimes of X_D and X_O excitons at ~1 ns and 500 ps, respectively. Notably, the X_D lifetime shows a nonmonotonic trend, first decreasing and then increasing, as the detuning changes from red to blue relative to the X_D one. In contrast, the X_O lifetime remains nearly constant across all detuning conditions. Also, the linewidths of X_D and X_O excitons exhibit distinct trends, as the energy between the gap plasmon mode and excitons is tuned, confirming the coupling between X_D and the gap plasmon mode (fig. S11).

Estimation of the intrinsic room-temperature lifetime of X_D

Figure 3A presents the ratio of the peak areas of X_D to X_O emission as a function of the energy detuning between the gap plasmon mode and X_D. The trend follows a Lorentzian profile with a linewidth of ~100 meV, closely matching the linewidth of the gap plasmon mode observed in the scattering spectrum (Fig. 1C). The energy splitting between X_O and X_D excitons is 57 ± 2.1 meV across the nanocavities studied. Notably, the X_D and X_O lifetimes depend differently on cavity-exciton detuning: As the detuning increases, the

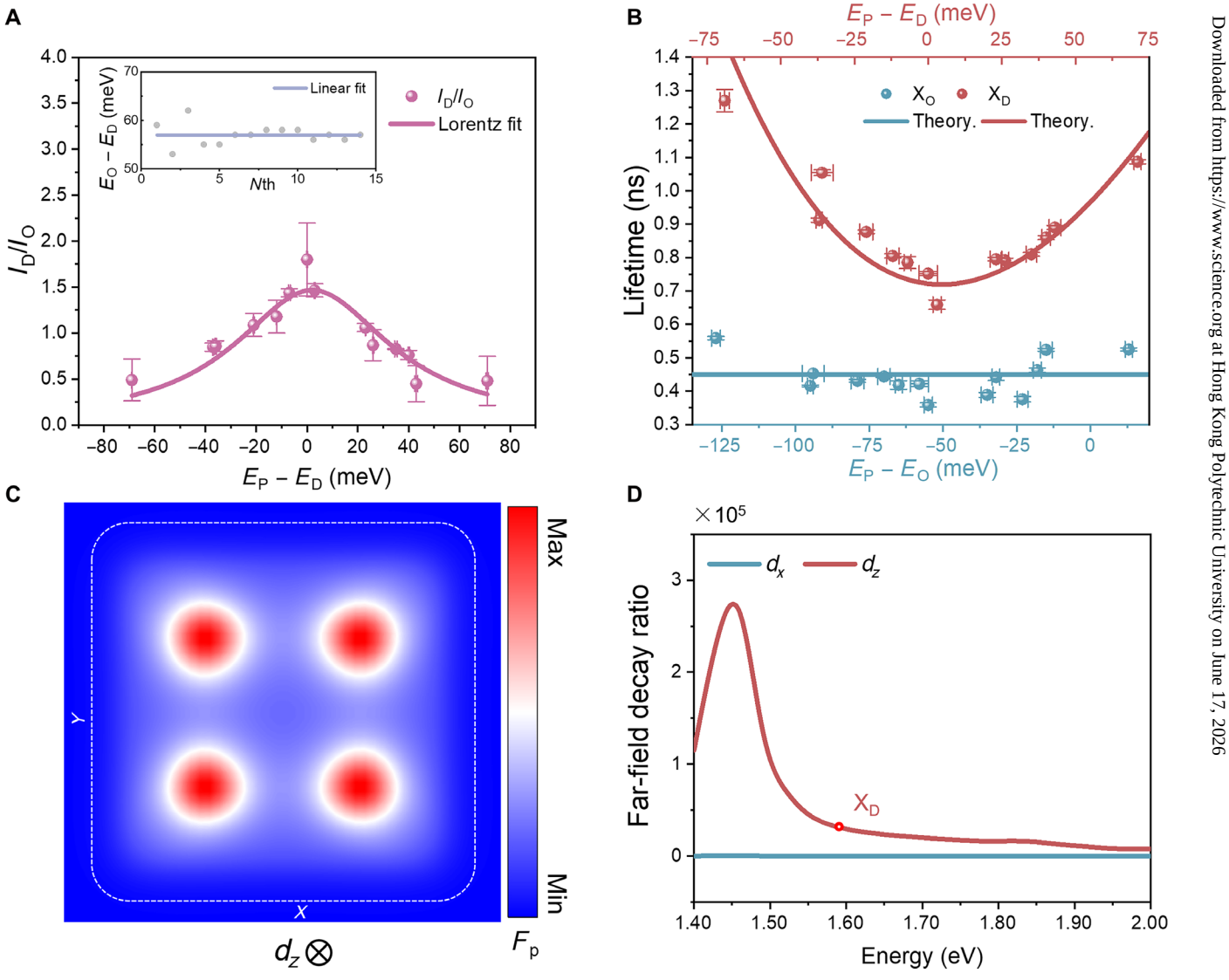

Fig. 3. Plasmonic tuning of the dark-exciton emission intensity and radiation dynamics. (**A**) Emission intensity ratio of X_D to X_O excitons as a function of energy detuning between the gap plasmon mode and the X_D resonance. The error bars represent the uncertainty in the parameter estimates. The solid line is the Lorentzian fit. The inset displays the energy splitting between X_O and X_D excitons across 14 nanocavities, with a mean value of 57 meV and an SD of 2.1 meV. (**B**) Measured lifetimes of the X_D (red dots) and X_O (blue dots) excitons as a function of energy detuning between the gap plasmon mode and the X_D or X_O resonances. The error bars for both axes are derived from the uncertainties in the fitting process. The solid line is calculated with Eq. 1. (**C**) Spatial distribution of the radiative decay rate enhancement at 1.59 eV in an NCoM nanocavity. The maximum Purcell factor (*F*p) of ~40,000 is observed at the locations close to the four corners of the nanocube. (**D**) Simulated spectra of the far-field radiative decay rate enhancement Γ_{FF}/Γ_0 for the in-plane (d_x) and out-of-plane (d_z) dipoles in the regions of the maximum Purcell enhancement.

X_D lifetime is significantly increased, whereas the X_O lifetime remains unchanged (Fig. 3B).

To explain the impact of dissipative cavity detuning on the X_D lifetime, we consider a cavity quantum electrodynamics model based on the Purcell formalism. Within this framework, when considering the weak coupling between dipole emitters and dissipative nanoresonators, the spontaneous decay rate Γ of an emitter in the cavity can be described as (*23*)

$$\Gamma = F\Gamma_0 \frac{\omega_0^2}{\omega^2} \frac{\omega_0^2}{\omega_0^2 + 4Q^2(\omega-\omega_0)^2}\left[1 + 2Q\frac{\omega-\omega_0}{\omega_0}\frac{\mathrm{Im}\left(\widetilde{V}\right)}{\mathrm{Re}\left(\widetilde{V}\right)}\right] \quad (1)$$

where ω is the emitter frequency, ω_0 is the resonant frequency of the cavity, and Γ_0 is the intrinsic X_D spontaneous decay rate in a bare WSe_2 ML. The quality factor of the cavity Q is defined as $\omega_0 / \Delta\omega$ with $\Delta\omega$ being the bandwidth of the cavity and $\widetilde{V}$ being the mode volume of the cavity, calculated accounting for dissipation (*24*). In addition, F signifies the generalized Purcell factor, which is determined as

$$F = \frac{3}{4\pi^2}\left(\frac{\lambda_0}{n}\right)^3 \mathrm{Re}\left(\frac{Q}{\widetilde{V}}\right) \quad (2)$$

where λ_0 is the X_D wavelength in the WSe_2 and n is the refractive index of a WSe_2 ML (*25*). Using the electromagnetic field distributions in the cavity calculated using the finite element method (see Materials and Methods for details), for the parameters of the NCoM used in the experiment, we obtain the following: $\frac{\widetilde{V}}{\lambda_0^3} = (1.93 - 0.02i) \times 10^{-7}$, $Q \approx 10$, $F \approx 3.3 \times 10^4$, and thus $\Gamma_0 \approx (4.2 \pm 0.4) \times 10^{-5}$ ns^{-1}. These estimates provide an excellent agreement with the experimental data (Fig. 2B). The error bar of Γ_0 indicates the variability of Γ_0 derived from fitting to the experimental data (fig. S14). On the basis of this, we deduce that the X_D lifetime in a bare WSe_2 ML at room temperature is ~24 ± 2.3 μs. To the best of our knowledge, this is the first reported estimation of the intrinsic radiative lifetime of X_D at room temperature.

The quasi-parabolic relationship between X_D lifetime and cavity detuning, described by Eq. 1, agrees well with the experimental findings obtained from multiple nanocavities (Fig. 3B). The optimal enhancement wavelength, at which the shortest lifetime is observed, is blue shifted (~5 meV) relative to the exciton emission energy as seen from the fit. This blue shift can be predominantly attributed to dissipation-induced spectral shifts in the NCoM cavity (see note S3 for detailed analysis). In addition, other factors may contribute, including the intrinsic blue shift between the exciton absorption and emission energies (*26*) and the typical blue shift of near-field resonance relative to far-field scattering in strongly coupled nanocavities (*27*). It is also important to consider that these experiments are inevitably affected by inhomogeneous broadening arising from variations in gap morphology and inherent local characteristics of WSe_2, leading to fluctuations across different samples. Moreover, the orthogonal polarizations of X_D and X_O dipoles result in markedly different mode volumes and thus the Purcell factors. Hence, the cavity-driven enhancement of the X_O emission is highly inefficient (Fig. 3B), resulting in the negligible dependence of the X_O lifetime on the detuning energy. A slight asymmetry in lifetime between positive and negative detuning was also observed, an expected feature of dissipative nanocavities (*23*). Notably, our findings reveal that dissipation is pivotal in the intricate dependency of X_D lifetime on detuning. Nevertheless, this NCoM cavity allows the reduction of the X_D lifetime down to ~650 ps (four orders of magnitude) while maintaining the intrinsic X_O lifetime at 444 ± 57ps.

To investigate the spatial distribution of the Purcell factor inside the cavity, we used the MNPBEM toolbox (*28*) to conduct the numerical simulations and compute the Purcell factor at the X_D energy (1.59 eV). A pronounced enhancement of the Purcell factor for out-of-plane dipole polarization was observed (Fig. 3C). The total decay rate Γ (fig. S13) is composed of both near-field and far-field components: $\Gamma = \Gamma_{FF} + \Gamma_{NF}$. When placing a dipole in the region of the maximum Purcell enhancement, the far-field decay rate as a function of the emission wavelength was simulated, showing different trends for the emitters with in-plane and out-of-plane polarization directions (Fig. 3D). The maximum intensity is observed around the X_D position, indicating a decay rate enhancement larger than 7000. Considering the fluctuations in the size and shape of the colloidal nanocubes, which can result in variations in the plasmon resonances of the WSe_2-NCoM cavities, it may be possible to achieve even larger on-resonance local density of optical states and radiation efficiency. This could further enhance the X_D emission rate. Compared to the in-plane dipole, the far-field radiative efficiency of the out-of-plane dipole in the NCoM cavity is much stronger (fig. S13). This also demonstrates the potential to overcome the intrinsic weak transition dipole moment of X_D excitons and manipulate their emission and dynamics at room temperature.

Directionality control of X_D radiation by nanocavity configurations

NCoM cavities, beyond modulating the radiation rate of excitons, also provide a flexible platform for effectively tailoring the far-field emission directionality of the excitons. Providing a direct visualization of the momentum space distribution, BFP imaging can be used to map the angular distribution of the emitted light (*29*). We first compare the radiation patterns of X_D and X_O in the WSe_2-NCoM nanocavity. Figure 4B shows the experimentally measured BFP images of X_D from a relatively flat WSe_2-NCoM nanocavity, which is verified by the corresponding scanning electron microscopy (SEM) micrographs in Fig. 4A, appearing to be a donut-like shape. However, the radiation pattern of X_O emission in the WSe_2-NCoM cavity is pie-like (Fig. 4E), which is barely modified by the gap plasmon mode. Moreover, the X_O emission exhibits a one-lobe radiation profile, which is obviously different from that of the donut-like X_D radiation pattern (two-lobe profile). The maximum X_D PL intensity is observed at ~±36°, whereas the X_O PL intensity is maximized at ~0°. The clear difference between the two excitons is seen in fig. S16, where the BFP intensities are azimuthally averaged in the in-plane directions (see Materials and Methods for details), confirming their orthogonal polarizations, with X_D oriented out-of-plane and X_O aligned in-plane. The 3D simulations of the gap plasmon mode I and transverse mode III also show completely opposite shapes of the radiation patterns, in agreement with the experimental results (fig. S16). These results provide clear evidence for the fundamentally different radiation characteristics of X_D and X_O excitons in the WSe_2-NCoM nanocavity.

Because of the plasmon-exciton coupling, the far-field emission directionality of X_D is influenced by the plasmon mode geometry. The radiation patterns of X_D could be either asymmetric (C) or

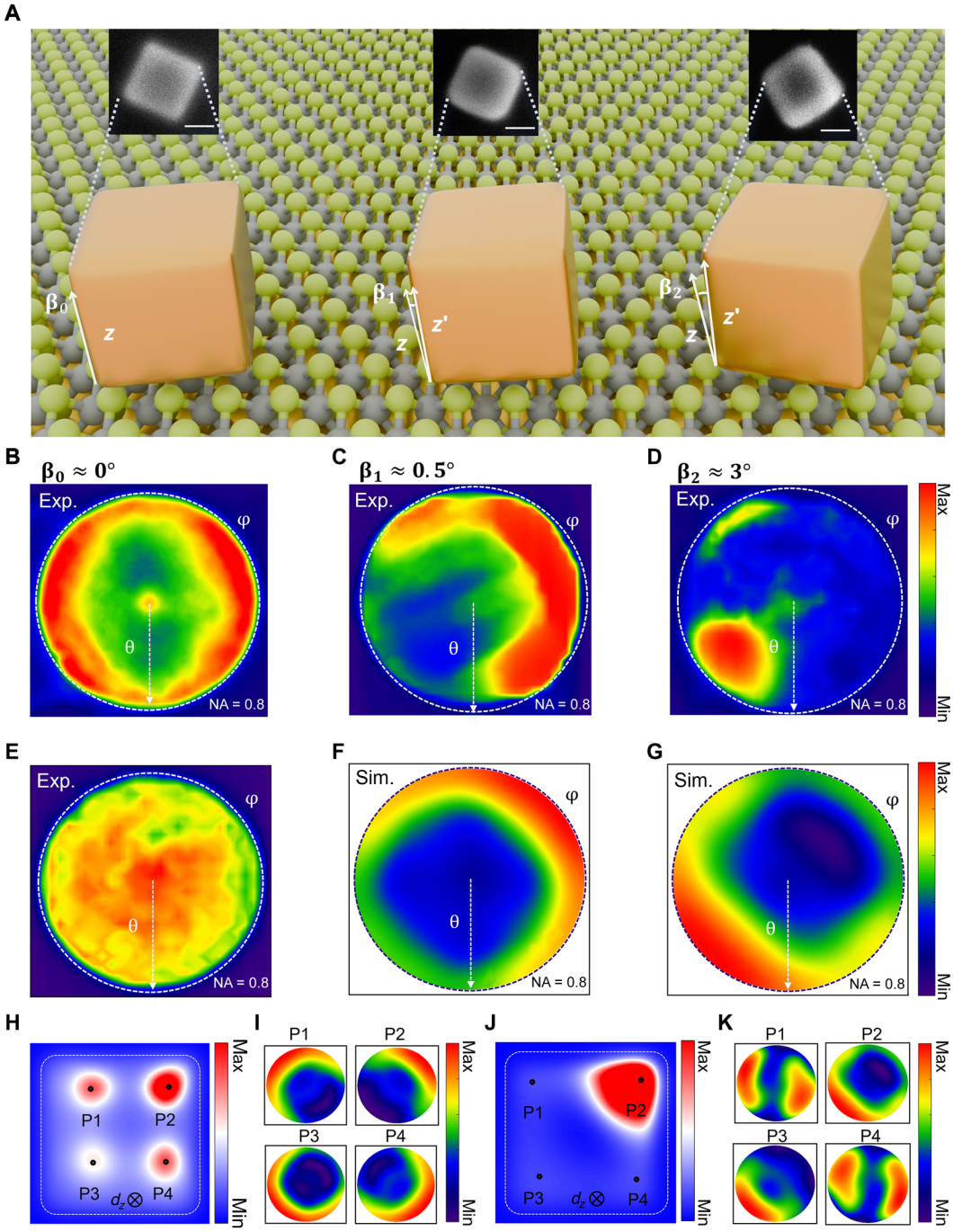

Fig. 4. Plasmonic tuning of the dark-exciton emission directionality. (**A**) Schematic illustration of three WSe_2-NCoM nanocavities with different orientations, where β_0, β_1, and β_2 denote the angles between the *z* axis and the normal (*z*′) of the top surface of each nanocube. Insets show SEM micrographs of the respective WSe_2-NCoM cavities. Scale bars, 50 nm. (**B** to **D**) BFP images of X_D radiation from three WSe_2-NCoM nanocavities: (A) for $\beta_0 \approx 0°$, (B) for $\beta_1 \approx 0.5°$, and (C) for $\beta_2 \approx 3°$, showing distinct patterns correlated with the nanocube orientation in Fig. 4A. The white dotted line represents the maximum angular collection range of the objective used in the experiments [numerical aperture (NA) = 0.8]. (**E**) Experimentally measured BFP image of X_O from WSe_2-NCoM nanocavities, showing a distinctly different pattern than for X_D exciton. (**F** and **G**) Simulated BFP images of X_D radiation for two different tilt angles, (F) for $\beta_1 \approx 0.5°$ and (G) for $\beta_2 \approx 3°$, accounting for the spatially redistributed Purcell factor within the plasmonic gap and the emitter radiation patterns in the corresponding hotspot positions. (**H**) Spatial distributions of the radiative decay rate enhancement at 1.59 eV in the NCoM nanocavity with tilt angle $\beta_1 \approx 0.5°$. P1 to P4 correspond to the positions of maximum Purcell factor located near the four corners of the nanocube. (**I**) Simulated BFP images for vertically oriented dipole emitters placed at the four hotspot positions [P1 to P4 in (H)] within the plasmonic gap, each located at a local Purcell factor maximum near a corner. All images are collected using the same objective (NA = 0.8). (**J**) Similar results as (H) but for the tilted angle of $\beta_2 \approx 3°$. (**K**) Similar results as (I) but for the tilted angle of $\beta_2 \approx 3°$.

corner like (D). In particular, the observed asymmetries of X_D radiation patterns in Fig. 4 (C and D) can be primarily attributed to the tilt of the nanocavities, which can substantially modify the angular emission profile of embedded dipole emitters (*30*, *31*). The SEM micrographs of the three WSe_2-NCoM nanocavities in Fig. 4A confirm their different orientations. These cavity-to-cavity variations arise primarily from the inherent randomness of the drop-casting process, along with the surface irregularities of ML WSe_2 and residual polymer left from the 2D material transfer process, resulting in the varied geometries and tilt angles. In the SEM images, brighter regions indicate higher secondary electron emission, closely related to the escape volume on the surface (fig. S17). This pronounced difference in the radiation patterns fundamentally arises from two main factors. First, even slight tilts result in substantial changes of the Purcell factor distribution (*32*), which exhibits either an asymmetric profile at a slight tilt (Fig. 4H; $\beta_1 \approx 0.5°$) or a corner-like pattern at a larger tilt (Fig. 4J; $\beta_2 \approx 3°$), with the hotspot shifting closer to the cavity edge as the tilt increases. Second, the far-field radiation patterns of dipoles located at different locations within the plasmonic gap vary markedly (Fig. 4, I and K) (*33*). The interplay of these two effects leads to a marked modulation in the directional emission of X_D but with negligible influence on the PL intensity (fig. S15). To accurately capture the overall radiation pattern from the tilted cavity, we consider four representative hotspot positions in the gap (P1 to P4), each corresponding to a local maximum of the Purcell factor near the nanocube corner. The radiation pattern at each point is weighted by its respective Purcell factor, and the sum yields the calculated BFP images shown in Fig. 4 (F and G). The emitter radiation pattern at the dominant Purcell factor hotspot (P2) exhibits a complete reversal between the two different tilt angles (*33*), leading to a distinct overall radiation pattern (Fig. 4, F and G). This demonstrates how subtle changes in nanocube orientation can effectively steer the emission directionality of X_D excitons in NCoM cavities, offering a strategy for directional control in nanophotonic systems. To achieve more precise control over its emission directionality, one possible approach is to modify the shape of the top nanoparticles, for example, replacing them with nanodecahedra (*34*) or other sharp-edged polyhedral geometries. These geometries have already been reported to exhibit pronounced directionality in dark-field scattering measurements.

DISCUSSION

At room temperature, we achieved four orders of magnitude reduction in the PL lifetime of spin-forbidden X_D in a WSe_2 monolayer coupled to a plasmonic nanocavity, making the X_D lifetime comparable to that of X_O. This is because the nanocavity selectively enhances the radiative decay rate of X_D, without noticeably altering that of X_O. According to a quantum electrodynamics model based on the Purcell formalism for dissipative cavities, we estimated the intrinsic room-temperature lifetime of X_D in a pristine WSe_2 monolayer to be ~24 ± 2.3 μs. Beyond the lifetime control, we further observed that the X_D radiation pattern highly depends on the nanocavity orientation and emitter location, which both govern the Purcell factor distribution within the nanogap and the emitter's far-field radiation pattern. Tilting the nanocavity allowed the donut-shape radiation pattern to transition into a corner-like shape, demonstrating the capacity to produce a nanoscale light source with high emission directionality. These findings demonstrate an effective approach for leveraging a single plasmonic nanostructure to control the X_D emission intensity, dynamics, and radiation directionality. The versatility of this easy-to-implement plasmonic approach, along with the proposed theoretical framework, offers new application prospects for the advancement of optoelectronic devices and quantum information systems based on 2D semiconductors.

MATERIALS AND METHODS

Sample fabrication

Gold substrates were prepared by depositing 100-nm-thick gold films at a rate of 0.5 Å/s on a silicon wafer template through electron beam deposition (PVD 75 Thin Film Deposition System, Kurt J. Lesker Company). To obtain a smooth gold film, silica substrates were bonded to the freshly evaporated gold using an ultraviolet (UV)–curable glue and template striped. The TMDC monolayer was mechanically exfoliated from bulk WSe_2 onto polydimethylsiloxane (PDMS). The monolayer structure was verified with the help of PL spectroscopy. Then, the monolayer WSe_2 was transferred onto a gold film using the all-dry viscoelastic stamping transfer method (*35*, *36*). UV light illumination for 20 min was used to eliminate the residual PDMS from the WSe_2 surface. The Au nanocubes were purchased from X-nanogold Ltd. To achieve stronger film confinement, the cetrimonium bromide protective layer was removed by centrifugation at 2500 rpm for 2 min (*37*). After ultrasonication for 5 min to ensure the uniform separation of single particles, the Au nanocubes were dispersed on the WSe_2 monolayer using the drop-casting method. The etched WSe_2-NCoM was obtained from the above structures by directional etching for 25 s using argon plasma bombardment (PVA IoN 7B; 20-W power) to remove WSe_2 not covered by the nanocubes. The operational pressure was 2 torr, and 2 standard cubic centimeter per minute flow rate of Ar gas was used to generate the plasma for etching.

Numerical simulation method

Electromagnetic simulations were performed using COMSOL Multiphysics V6.1 software, based on the finite element method. The permittivity of gold was taken from (*38*). A perfectly matched layer was used to enclose the computational domain to minimize unwanted reflections at the domain boundaries. The scattering spectra of the nanocavity were derived by integrating the upward scattering power flow within an angle of 106°, corresponding to the numerical aperture (NA) of 0.8 of the objective lens used in the experiments. The meshing of the simulation models, particularly in the gap region, was carefully refined to ensure computational convergence.

Coupled oscillator model

LSP mode was modeled as a bright mode that can directly couple with the incident light, while the excitons do not interact with light directly. Assuming no coupling between the two excitons, the plasmon-exciton coupled system can be treated as an external-force–driven oscillator (LSP) coupled with internal oscillators (excitons). In this framework, the light scattering in the two-oscillator system (LSP-exciton) can be described as (*22, 39*)

$$\sigma_{sca} = A \cdot E^4 \left| \frac{E^2 - E_0^2 + i\Gamma_0 E}{\left(E^2 - E_0^2 + i\Gamma_0 E\right)\left(E^2 - E_p^2 + i\Gamma_p E\right) - 4\kappa^2 E^2} \right|^2 \quad (3)$$

where A is the scattering amplitude; E_p and E_0 are the resonant energies of the gap plasmon mode and bright exciton X_O; Γ_p and Γ_0 are the dissipation rate of the gap plasmon mode and X_O exciton, respectively; κ is

the coupling strength between the gap plasmon mode and X_O exciton; and σ_{sca} is the scattering intensity at the energy E.

Purcell factor calculations with boundary element method

To calculate the spontaneous decay rate of a quantum emitter in an NCoM cavity, we use the MATLAB toolbox MNPBEM to solve the Maxwell's equations (*28*). A gold nanocube with a size of 85 nm is placed 1.8 nm above a gold mirror. An in-plane (d_x) and out-of-plane (d_z) dipoles are located between the nanocube and the mirror, representing bright and dark excitons, respectively. The total decay rate γ of a quantum emitter in a cavity is expressed as

$$\gamma = \gamma^{\text{free}} + \frac{6\pi\varepsilon_0\gamma^{\text{free}}}{|r|^2 k^3}\text{Im}\left\{d^* \cdot E_s\left(r_0\right)\right\} \quad (4)$$

where γ^{free} is the free-space decay rate, $|r|$ is the distance between the position of the dipole and a reference point in the cavity or environment, k is the wave number, d is the transition dipole moment, and $E_s\left(r_0\right)$ is the induced secondary electric field at the position of the dipole. In addition, the far-field radiative decay rate γ^{FF} is calculated by integrating the outgoing Poynting vector in the far-field zone over a unit sphere.

Optical spectroscopy

The dark-field scattering spectra of Au nanocubes were obtained using a home-built multifunctional spectroscopy and imaging system comprising a microscope system (BX53, Olympus) with a 100× dark-field objective, a spectrometer (Shamrock 500i, Andor), and a charge-coupled device (CCD) camera (Newton CCD BEX2-DD, Andor). Individual gold nanocubes were illuminated by a halogen lamp, and the scattered light was collected by the objective for spectral analysis. A standard diffuser is used as a reference to normalize the white light scattering. PL spectra of the pristine WSe_2 and the WSe_2-NCoM (Fig. 1) were obtained using a commercial confocal Raman system (WITec Raman alpha300) with a 100× objective (Zeiss LD EC Epiplan-Neofluar Dic; NA = 0.75). A linearly polarized continuous-wave (CW) laser with a wavelength of 532 nm and an intensity of 25 W/cm^2 was used as the excitation source. TRPL spectra (Fig. 2) were measured using the second harmonic of the Ti: sapphire femtosecond laser (Chameleon Ultra II, Coherent) output at 1064 nm (pulse duration ~ 120 fs) with a repetition rate of 80 MHz (fig. S2). The PL signal from the WSe_2-NCoM cavity in the focal plane is collected by the same objective. It is then directed into the detection path by a short-pass dichroic mirror, which blocks the pump laser while allowing the PL signal to pass through. A 785 ± 5–nm band-pass filter was used to select the emission of dark excitons. The signal was registered by a single-photon detector [PDM Series, Micro Photon Devices (MPD)]. The output of the MPD was recorded in the PicoHarp 300 system for time-correlated single photon counting measurements. BFP measurements of the PL emission from WSe_2-NCoM were performed under a 532-nm CW laser excitation through a 100× objective LMPlan with NA = 0.8. To obtain an azimuthally averaged relation between the emission intensity and the polar angle θ in the BFP images, the map was divided into rings corresponding to different θ values. Then, the intensity within each ring was integrated and normalized to the area of the ring

$$I_{\text{average}}(\theta) = \frac{\int_0^{2\pi}\int_{\theta}^{\theta+\Delta\theta} R(\theta)\, I(\theta,\varphi)\, d\theta d\varphi}{\pi\left[R(\theta+\Delta\theta)^2 - R(\theta)^2\right]} \quad (5)$$

where $R(\theta)$ is the distance between the point and the center of the BFP image and $I(\theta, \varphi)$ is the BFP intensity at the position (θ, φ).

SEM characterizations

SEM was performed using a Helios 5 CX DualBeam microscope equipped with a field-emission gun. The accelerating voltage was set to 5 kV, and a working distance of ~4 mm was maintained. Samples were mounted with conductive carbon tape to enhance conductivity. Imaging was conducted using a secondary electron detector at a magnification of ×80,000 under high-vacuum conditions.

Supplementary Materials

This PDF file includes:

Notes S1 to S3
Figs. S1 to S18
References

REFERENCES

1. G.-B. Liu, W.-Y. Shan, Y. Yao, W. Yao, D. Xiao, Three-band tight-binding model for monolayers of group-VIB transition metal dichalcogenides. *Phys. Rev. B* **88**, 085433 (2013).
2. K. Kośmider, J. W. González, J. Fernández-Rossier, Large spin splitting in the conduction band of transition metal dichalcogenide monolayers. *Phys. Rev. B* **88**, 245436 (2013).
3. J. P. Echeverry, B. Urbaszek, T. Amand, X. Marie, I. C. Gerber, Splitting between bright and dark excitons in transition metal dichalcogenide monolayers. *Phys. Rev. B* **93**, 121107 (2016).
4. C. T. Yip, T. W. Lo, S.-C. Zhu, G. Y. Jia, H. Sun, C.-H. Lam, D. Lei, Tight-binding modeling of excitonic response in van der Waals stacked 2D semiconductors. *Nanoscale Horiz.* **4**, 969–974 (2019).
5. X.-X. Zhang, Y. You, S. Y. F. Zhao, T. F. Heinz, Experimental evidence for dark excitons in monolayer WSe_2. *Phys. Rev. Lett.* **115**, 257403 (2015).
6. M. R. Molas, C. Faugeras, A. O. Slobodeniuk, K. Nogajewski, M. Bartos, D. M. Basko, M. Potemski, Brightening of dark excitons in monolayers of semiconducting transition metal dichalcogenides. *2D Mater.* **4**, 021003 (2017).
7. T. Smoleński, T. Kazimierczuk, M. Goryca, P. Wojnar, P. Kossacki, Mechanism and dynamics of biexciton formation from a long-lived dark exciton in a CdTe quantum dot. *Phys. Rev. B* **91**, 155430 (2015).
8. K.-D. Park, T. Jiang, G. Clark, X. Xu, M. B. Raschke, Radiative control of dark excitons at room temperature by nano-optical antenna-tip Purcell effect. *Nat. Nanotechnol.* **13**, 59–64 (2018).
9. C. Robert, T. Amand, F. Cadiz, D. Lagarde, E. Courtade, M. Manca, T. Taniguchi, K. Watanabe, B. Urbaszek, X. Marie, Fine structure and lifetime of dark excitons in transition metal dichalcogenide monolayers. *Phys. Rev. B* **96**, 155423 (2017).
10. X.-X. Zhang, T. Cao, Z. Lu, Y.-C. Lin, F. Zhang, Y. Wang, Z. Li, J. C. Hone, J. A. Robinson, D. Smirnov, S. G. Louie, T. F. Heinz, Magnetic brightening and control of dark excitons in monolayer WSe2. *Nat. Nanotechnol.* **12**, 883–888 (2017).
11. G. Wang, C. Robert, M. M. Glazov, F. Cadiz, E. Courtade, T. Amand, D. Lagarde, T. Taniguchi, K. Watanabe, B. Urbaszek, X. Marie, In-plane propagation of light in transition metal dichalcogenide monolayers: Optical selection rules. *Phys. Rev. Lett.* **119**, 047401 (2017).
12. D. J. Roth, P. Ginzburg, L. M. Hirvonen, J. A. Levitt, M. E. Nasir, K. Suhling, D. Richards, V. A. Podolskiy, A. V. Zayats, Singlet–triplet transition rate enhancement inside hyperbolic metamaterials. *Laser Photonics Rev.* **13**, 1900101 (2019).
13. Y. Zhou, G. Scuri, D. S. Wild, A. A. High, A. Dibos, L. A. Jauregui, C. Shu, K. De Greve, K. Pistunova, A. Y. Joe, T. Taniguchi, K. Watanabe, P. Kim, M. D. Lukin, H. Park, Probing dark excitons in atomically thin semiconductors via near-field coupling to surface plasmon polaritons. *Nat. Nanotechol.* **12**, 856–860 (2017).
14. T. W. Lo, X. Chen, Z. Zhang, Q. Zhang, C. W. Leung, A. V. Zayats, D. Lei, Plasmonic nanocavity induced coupling and boost of dark excitons in monolayer WSe_2 at room temperature. *Nano Lett.* **22**, 1915–1921 (2022).
15. Q. H. Wang, K. Kalantar-Zadeh, A. Kis, J. N. Coleman, M. S. Strano, Electronics and optoelectronics of two-dimensional transition metal dichalcogenides. *Nat. Nanotechnol.* **7**, 699–712 (2012).
16. Z. Ye, T. Cao, K. O'Brien, H. Zhu, X. Yin, Y. Wang, S. G. Louie, X. Zhang, Probing excitonic dark states in single-layer tungsten disulphide. *Nature* **513**, 214–218 (2014).
17. Z. Wang, L. Liu, D. Zhang, A. V. Krasavin, J. Zheng, C. Pan, E. He, Z. Wang, S. Zhong, Z. Li, M. Ren, X. Guo, A. V. Zayats, L. Tong, P. Wang, Effect of mirror quality on optical response of nanoparticle-on-mirror plasmonic nanocavities. *Adv. Opt. Mater.* **11**, 2201914 (2023).
18. X. Li, L. Zhou, Z. Hao, Q. Wang, Plasmon–exciton coupling in complex systems. *Adv. Opt. Mater.* **6**, 1800275 (2018).

19. N. S. Mueller, R. Arul, G. Kang, A. P. Saunders, A. C. Johnson, A. Sánchez-Iglesias, S. Hu, L. A. Jakob, J. Bar-David, B. De Nijs, L. M. Liz-Marzán, F. Liu, J. J. Baumberg, Photoluminescence upconversion in monolayer WSe_2 activated by plasmonic cavities through resonant excitation of dark excitons. *Nat. Commun.* **14**, 5726 (2023).
20. O. A. Ajayi, J. V. Ardelean, G. D. Shepard, J. Wang, A. Antony, T. Taniguchi, K. Watanabe, T. F. Heinz, S. Strauf, X.-Y. Zhu, J. C. Hone, Approaching the intrinsic photoluminescence linewidth in transition metal dichalcogenide monolayers. *2D Mater.* **4**, 031011 (2017).
21. H. Wei, X. Yan, Y. Niu, Q. Li, Z. Jia, H. Xu, Plasmon–exciton interactions: Spontaneous emission and strong coupling. *Adv. Funct. Mater.* **31**, 2100889 (2021).
22. T. W. Lo, Q. Zhang, M. Qiu, X. Guo, Y. Meng, Y. Zhu, J. J. Xiao, W. Jin, C. W. Leung, D. Lei, Thermal redistribution of exciton population in monolayer transition metal dichalcogenides probed with plasmon–exciton coupling spectroscopy. *ACS Photonics* **6**, 411–421 (2019).
23. C. Sauvan, J. P. Hugonin, I. S. Maksymov, P. Lalanne, Theory of the spontaneous optical emission of nanosize photonic and plasmon resonators. *Phys. Rev. Lett.* **110**, 237401 (2013).
24. T. Wu, M. Gurioli, P. Lalanne, Nanoscale light confinement: The Q's and V's. *ACS Photonics* **8**, 1522–1538 (2021).
25. G.-H. Jung, S. Yoo, Q.-H. Park, Measuring the optical permittivity of two-dimensional materials without a priori knowledge of electronic transitions. *Nanophotonics* **8**, 263–270 (2019).
26. M. Palummo, M. Bernardi, J. C. Grossman, Exciton radiative lifetimes in two-dimensional transition metal dichalcogenides. *Nano Lett.* **15**, 2794–2800 (2015).
27. A. Lombardi, A. Demetriadou, L. Weller, P. Andrae, F. Benz, R. Chikkaraddy, J. Aizpurua, J. J. Baumberg, Anomalous spectral shift of near- and far-field plasmonic resonances in nanogaps. *ACS Photonics* **3**, 471–477 (2016).
28. J. Waxenegger, A. Trügler, U. Hohenester, Plasmonics simulations with the MNPBEM toolbox: Consideration of substrates and layer structures. *Comput. Phys. Commun.* **193**, 138–150 (2015).
29. Z. Sun, J. Gu, A. Ghazaryan, Z. Shotan, C. R. Considine, M. Dollar, B. Chakraborty, X. Liu, P. Ghaemi, S. Kéna-Cohen, V. M. Menon, Optical control of room-temperature valley polaritons. *Nat. Photonics* **11**, 491–496 (2017).
30. S. I. Bogdanov, M. Y. Shalaginov, A. S. Lagutchev, C.-C. Chiang, D. Shah, A. S. Baburin, I. A. Ryzhikov, I. A. Rodionov, A. V. Kildishev, A. Boltasseva, V. M. Shalaev, Ultrabright room-temperature sub-nanosecond emission from single nitrogen-vacancy centers coupled to nanopatch antennas. *Nano Lett.* **18**, 4837–4844 (2018).
31. H. Chen, Z. Jiang, H. Hu, B. Kang, B. Zhang, X. Mi, L. Guo, C. Zhang, J. Li, J. Lu, L. Yan, Z. Fu, Z. Zhang, H. Zheng, H. Xu, Sub-50-ns ultrafast upconversion luminescence of a rare-earth-doped nanoparticle. *Nat. Photonics* **16**, 651–657 (2022).
32. X. Qi, T. W. Lo, D. Liu, L. Feng, Y. Chen, Y. Wu, H. Ren, G.-C. Guo, D. Lei, X. Ren, Effects of gap thickness and emitter location on the photoluminescence enhancement of monolayer MoS_2 in a plasmonic nanoparticle-film coupled system. *Nanophotonics* **9**, 2097–2105 (2020).
33. M. J. Horton, O. S. Ojambati, R. Chikkaraddy, W. M. Deacon, N. Kongsuwan, A. Demetriadou, O. Hess, J. J. Baumberg, Nanoscopy through a plasmonic nanolens. *Proc. Natl. Acad. Sci. U.S.A.* **117**, 2275–2281 (2020).
34. S. Hu, E. Elliott, A. Sánchez-Iglesias, J. Huang, C. Guo, Y. Hou, M. Kamp, E. S. A. Goerlitzer, K. Bedingfield, B. De Nijs, J. Peng, A. Demetriadou, L. M. Liz-Marzán, J. J. Baumberg, Full control of plasmonic nanocavities using gold decahedra-on-mirror constructs with monodisperse facets. *Adv. Sci.* **10**, e2207178 (2023).
35. J. Sun, H. Hu, D. Zheng, D. Zhang, Q. Deng, S. Zhang, H. Xu, Light-emitting plexciton: Exploiting plasmon–exciton interaction in the intermediate coupling regime. *ACS Nano* **12**, 10393–10402 (2018).
36. H. Gao, Y. Hu, Y. Xuan, J. Li, Y. Yang, R. V. Martinez, C. Li, J. Luo, M. Qi, G. J. Cheng, Large-scale nanoshaping of ultrasmooth 3D crystalline metallic structures. *Science* **346**, 1352–1356 (2014).
37. G.-C. Li, Q. Zhang, S. A. Maier, D. Lei, Plasmonic particle-on-film nanocavities: A versatile platform for plasmon-enhanced spectroscopy and photochemistry. *Nanophotonics* **7**, 1865–1889 (2018).
38. P. B. Johnson, R. W. Christy, Optical constants of the noble metals. *Phys. Rev. B* **6**, 4370–4379 (1972).
39. D. Zheng, S. Zhang, Q. Deng, M. Kang, P. Nordlander, H. Xu, Manipulating coherent plasmon–exciton interaction in a single silver nanorod on monolayer WSe_2. *Nano Lett.* **17**, 3809–3814 (2017).
40. E. J. Sie, A. Steinhoff, C. Gies, C. H. Lui, Q. Ma, M. Rösner, G. Schönhoff, F. Jahnke, T. O. Wehling, Y.-H. Lee, J. Kong, P. Jarillo-Herrero, N. Gedik, Observation of exciton redshift–blueshift crossover in monolayer WS_2. *Nano Lett.* **17**, 4210–4216 (2017).
41. R. Chikkaraddy, B. De Nijs, F. Benz, S. J. Barrow, O. A. Scherman, E. Rosta, A. Demetriadou, P. Fox, O. Hess, J. J. Baumberg, Single-molecule strong coupling at room temperature in plasmonic nanocavities. *Nature* **535**, 127–130 (2016).
42. I. A. M. Al-Ani, K. As'ham, O. Klochan, H. T. Hattori, L. Huang, A. E. Miroshnichenko, Recent advances on strong light-matter coupling in atomically thin TMDC semiconductor materials. *J. Opt.* **24**, 053001 (2022).
43. J. Cuadra, D. G. Baranov, M. Wersäll, R. Verre, T. J. Antosiewicz, T. Shegai, Observation of tunable charged exciton polaritons in hybrid monolayer WS_2 – Plasmonic nanoantenna system. *Nano Lett.* **18**, 1777–1785 (2018).
44. G.-H. Peng, P.-Y. Lo, W.-H. Li, Y.-C. Huang, Y.-H. Chen, C.-H. Lee, C.-K. Yang, S.-J. Cheng, Distinctive signatures of the spin- and momentum-forbidden Dark exciton states in the photoluminescence of strained WSe_2 monolayers under thermalization. *Nano Lett.* **19**, 2299–2312 (2019).
45. A. M. Dadgar, D. Scullion, K. Kang, D. Esposito, E. H. Yang, I. P. Herman, M. A. Pimenta, E.-J. G. Santos, A. N. Pasupathy, Strain engineering and raman spectroscopy of monolayer transition metal dichalcogenides. *Chem. Mater.* **30**, 5148–5155 (2018).
46. Z. Peng, X. Chen, Y. Fan, D. J. Srolovitz, D. Lei, Strain engineering of 2D semiconductors and graphene: From strain fields to band-structure tuning and photonic applications. *Light Sci. Appl.* **9**, 190 (2020).
47. S. Rai, A. Srivastava, Low-temperature photoluminescence and Raman study of monolayer WSe2 for photocarrier dynamics and thermal conductivity. *J. Appl. Phys.* **136**, 154301 (2024).
48. M. Manca, M. M. Glazov, C. Robert, F. Cadiz, T. Taniguchi, K. Watanabe, E. Courtade, T. Amand, P. Renucci, X. Marie, G. Wang, B. Urbaszek, Enabling valley selective exciton scattering in monolayer WSe_2 through upconversion. *Nat. Commun.* **8**, 14927 (2017).
49. M. Liu, M. Pelton, P. Guyot-Sionnest, Reduced damping of surface plasmons at low temperatures. *Phys. Rev. B* **79**, 035418 (2009).
50. X. Xia, H. Huang, S. Li, R. Ai, Z. Tian, F. Yan, L. Shao, J. Wang, Switching on dark excitons in WSe_2 monolayer at room temperature with plasmonic au nanodisk-on-mirror cavities. *Laser Photonics Rev.* **19**, e02012 (2025).
51. Q. Zhang, G.-C. Li, T. W. Lo, D. Y. Lei, Polarization-resolved optical response of plasmonic particle-on-film nanocavities. *J. Opt.* **20**, 024010 (2018).

Acknowledgments: We thank J. J. Baumberg from NanoPhotonics Centre, Cavendish Laboratory, Department of Physics, University of Cambridge, for the discussion of the analysis of asymmetric X_D radiation patterns; X. Zhao and J. B. Xu from Department of Electronic Engineering, and The Chinese University of Hong Kong, for the assistance of etching WSe_2-NCoM nanocavities. **Funding:** S.J., F.L., I.R., Y.W., Z.P., and D.L. acknowledge the financial support from the Research Grants Council of Hong Kong through a General Research Fund grant (grant no. 11309623) and an Area of Excellence grant (grant no. AoE/P-701/20) and from the City University of Hong Kong through an RMGS grant (grant no. 9229137) and an SRG project (grant no. 7005945). W.Y. acknowledges support by the National Natural Science Foundation of China (No. 12425406) and New Cornerstone Science Foundation. A.V.Z. acknowledges the support from the UK EPSRC grant UKRI3056. T.W.L. acknowledges the support from the Royal Society through the Newton International Fellowship. **Author contributions:** Conceptualization: S.J., F.L., T.W.L., and D.L. Methodology: S.J., F.L., T.W.L., I.R., and D.L. Investigation: S.J., K.L., Y.Z., A.V.Z., and D.L. Visualization: S.J., F.L., I.R., and D.L. Resources: A.V.Z., S.J., and D.L. Funding acquisition: W.Y., A.V.Z., and D.L. Formal analysis: S.J., F.L., I.R., Z.P., W.Y., A.V.Z., and D.L. Data curation: S.J. and F.L. Project administration: S.J. and D.L. Software: F.L., I.R., and Y.W. Supervision: A.V.Z. and D.L. Writing—original draft: S.J., F.L., A.V.Z., and D.L. Writing—review and editing: S.J., F.L., I.R., T.W.L., Y.W., Z.P., K.L., W.Y., A.V.Z., and D.L. **Competing interests:** The authors declare that they have no competing interests. **Data and materials availability:** All data and code needed to evaluate and reproduce the results in the paper are present in the paper and/or the Supplementary Materials.

Submitted 13 July 2025
Accepted 11 December 2025
Published 16 January 2026
10.1126/sciadv.aea5781

ScienceAdvances

Plasmonic tuning of dark-exciton radiation dynamics and far-field emission directionality in monolayer WSe_2

Shuaiyu Jin, Feihong Liu, Ilya Razdolski, Tsz Wing Lo, Yaorong Wang, Zhiwei Peng, Kuan Liang, Ye Zhu, Wang Yao, Anatoly V. Zayats, and Dangyuan Lei

Sci. Adv. **12** (3), eaea5781. DOI: 10.1126/sciadv.aea5781

Science Advances (ISSN 2375-2548) is published by the American Association for the Advancement of Science. 1200 New York Avenue NW, Washington, DC 20005. The title *Science Advances* is a registered trademark of AAAS.